ORIGINAL PAPER

Characterization of Bi$_2$Se$_3$ prepared by electrodeposition

M. Khadiri[1] · M. Elyaagoubi[2] · R. Idouhli[1] · M. Mabrouki[3] · A. Abouelfida[1] · A. Outzourhit[2]

Abstract

Bi$_2$Se$_3$ compound was deposited catholically under potential control, from a mixture solution composed from equimolar SeO$_2$ and BiCl$_3$. The concentration of selenium and bismuth precursors was about $5 \cdot 10^{-3}$ M. The electrodeposited films were grown on FTO substrates (Transparent Conductive Glass Fluorine-Doped Tin Oxide (FTO)–Coated Glass). Deposition potential was determined from cyclic voltammetry (CV) where the platinum mesh was taken as working electrode. The growth kinetics depends on the applied potential. It was found, using EDS technique, that suitable ratio of Se/Bi corresponding to Bi$_2$Se$_3$ was reached at -250 mV vs. SCE (saturated calomel electrode). X-ray and grazing X-ray diffraction revealed that the obtained film at -250 and -200 mV/SCE consisted a rhombohedral Bi$_2$Se$_3$ structure. Raman shift was employed to corroborate the X-ray results with the possibility of formation of a rhombohedral Bi$_2$Se$_3$ when the applied potential was -200 mV (vs. SCE). The Bi$_2$Se$_3$-obtained films were an n-type semiconductor with a carrier charge concentration which depends on the applied potential.

Keywords Bi$_2$Se$_3$ · Cyclic voltammetry · Electrodeposition · Nucleation · Thin films

Introduction

Groups V–VI thin-film semiconductors based on sulfides, selenides, and tellurides have a narrow band gap. Among them, the bismuth selenide (Bi$_2$Se$_3$) is a direct gap semiconductor, and the gap energy noted E_g ranges from 0.16 to 0.35 eV [1]. Bismuth selenide has been widely studied because of its non-toxicity [2] and its potential applications in medical [3], photovoltaic [4], infrared, and gas detection [5], and in thermoelectric and optoelectronic devices applications fields [6–8].

Bismuth selenide (Bi$_2$Se$_3$) has a rhombohedral crystal structure, integrated in a hexagonal lattice which allows to highlight the stacking of atomic layers, corresponding to the basic quintet of the structure: Se(1)-Bi-Se(2)-Bi-Se(1) [9]. The different atomic layers of the sequence are arranged perpendicularly to the ternary axis of the rhombohedral mesh, which is also the **c** axis of the hexagonal mesh. However, under particular preparation conditions, the orthorhombic phase may appear [10, 11]. Several techniques can be used to obtain Bi$_2$Se$_3$ thin films, namely exfoliation [8], radio frequency sputtering [12, 13], hydrothermal method [14, 15], co-reduction [16], successive ionic layer adsorption and reaction (SILAR) technique [17], potentiostatically controlled electroplating in HNO$_3$ medium at different voltages and on different substrates [10, 18–20], and electroplating under galvanostatic control [21].

In this work, we prepared thin films of Bi$_2$Se$_3$ by potentiostatic electrodeposition on an FTO-coated glass substrate in an acidic medium (HCl 1 M). The voltammetric study allowed us to determine the range of applied potential to obtain Bi$_2$Se$_3$ films. Several techniques are used for the characterization of the obtained films such as X-ray diffraction, scanning electron microscopy coupled with the energy dispersive X-ray (EDX) microanalysis. Vibration modes relative to the Bi$_2$Se$_3$ structure are determined by Raman spectroscopy.

✉ M. Khadiri
Khadiri_m@gmx.fr

1 Applied Chemistry and Biomass Laboratory Department of Chemistry, Faculty of Science Semlalia, University Cadi Ayyad, BP 2390, Morocco, Morocco

2 Laboratory of Nanomaterials for Energy and the Environment (LN2E), Faculty of Sciences Semlalia Marrakech, Cadi Ayyad University, BP 2390, Marrakech, Morocco

3 Laboratory of Industrial Engineering Beni-Mellal TSF, BP 523, 23000 Marrakech, Morocco

Experimental section

The study is carried out in a double-walled cell for temperature regulation. The selected temperature is 30 °C. The recording of the cyclic voltammetry (CV) and the chronoamperometric curves were carried out using a potentiostat/galvanostat type PZC 301, with a conventional three-electrode assembly. The cyclic voltammograms were obtained with a scanning speed of 100 mV/s. The deposition time is fixed at 1 h. The solution is a mixture of hydrochloric acid and DMSO in a volume ratio (90:10) respectively, to reach a concentration of HCl equal to 1 M. The bismuth precursor is $BiCl_3$, while the selenium oxide SeO_2 was the selenium precursor. The concentration used for bismuth and selenium is of the order of $5 \cdot 10^{-3}$ M. During electrochemical study, the solution was aerated and moderately stirred. Film deposition is obtained by applying a fixed potential. During the electrodeposition process, the evolution of the current against time was recorded. This deposition is grown on FTO substrates (Transparent Conductive Glass Fluorine-Doped Tin Oxide (FTO)–Coated Glass). Before electroplating, the FTO substrates are washed with water and liquid soap and then rinsed with water. Afterwards, the substrates are washed in two baths consisting of water/ethanol and water/acetone in an ultrasonic device. Afterwards, the FTO substrates are rinsed with distilled water. The surface exposed to the solution is 1 cm^2. Impedance spectroscopy and the capacitance measurements at a frequency of 1 kHz were carried out in Na_2SO_4 10^{-1} M solution. The characterization of the obtained films is carried out by normal and grazing incidence X-ray diffraction (Rigaku, Smart Lab SE). Raman spectroscopy is used for the characterization of the films obtained using an excitation source of the order of 532 nm (Confotec MR520). The composition and morphology of the obtained films are given using scanning electron microscopy (TESCAN VEGA3 SEM) coupled with an energy dispersive X-ray microanalysis system (EDAX, EDX).

Results and discussion

Figure 1 shows the cyclic voltammetry curves of the different solutions in 1 M HCl with 10% DMSO, obtained with a scanning speed of 100 mV/s. An anodic activity is observed in the case of a solution containing bismuth ($E_{p1} = -50$ mV (vs. SCE)). The CV curve of the mixture solution (bismuth and selenium solution) presented an anodic peak at $Ep_2 = 235$ mV (vs. SCE).

In the case of the bismuth solution, it is possible to attribute this anodic peak to the oxidation of bismuth to bismuth (III) [22, 23] according to the following reaction (Eq. 1):
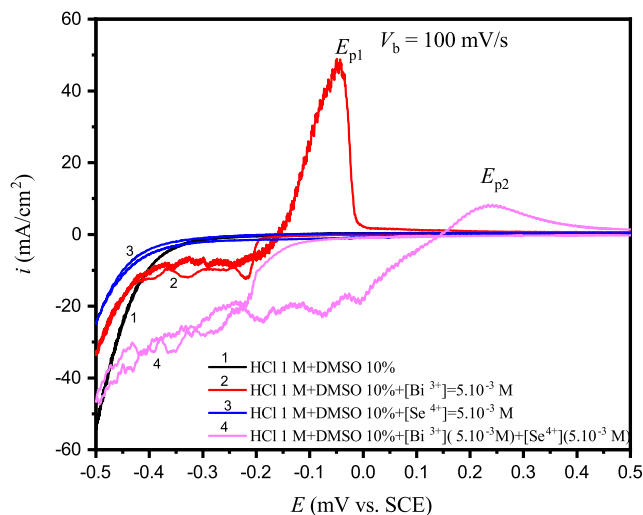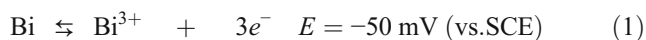
$$Bi \ \leftrightarrows \ Bi^{3+} \ + \ 3e^- \quad E = -50 \text{ mV (vs.SCE)} \quad (1)$$

Fig. 1 Cyclic voltammetry of bismuth, selenium and mixture bismuth-selenium solutions (Vb = 100 mV/s)

This theoretical value coincides with that determined from Fig. 1. During the reduction, it seems that from -190 mV/SCE, there is a reduction of Bi^{3+} into Bi, the diffusion step extends from -190 to -420 mV (vs. SCE) (Fig. 2).

In Fig. 3, we report the CV curve of selenium in acidic solution. The reduction peak centered at $+400$ mV (vs. SCE) may be attributed to the reduction of H_2SeO_3 to selenium (0) [22, 24] according to the following reaction:

$$H_2SeO_3 + 4H^+ + 4e^- \ \leftrightarrows \ Se_{(s)} + 3H_2O \quad (2)$$
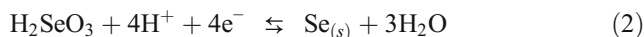
A slight change in the curve is observed between -270 and 60 mV (vs. SCE) and may be due to a pre-deposition of selenium (0) on the substrate at the same time as the selenium deposited from reaction (1) [25–27].

Once again, we are witnessing a change in the course of the CV curve relative to selenium, and which may be due to the
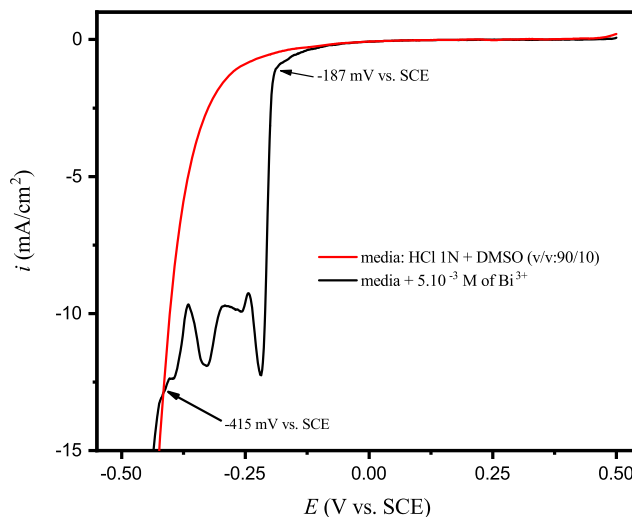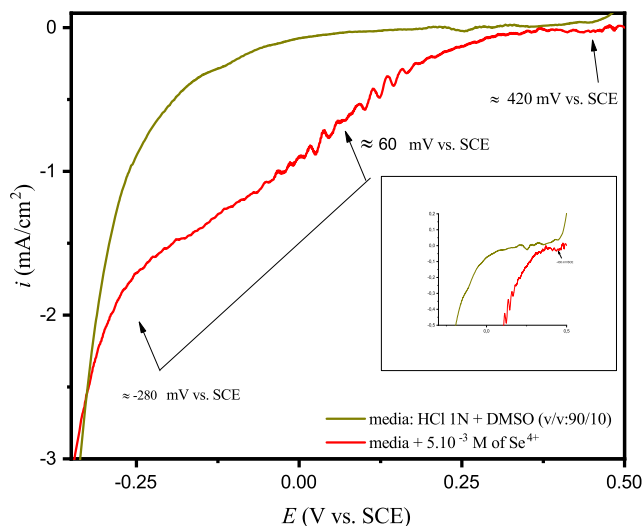

**Fig. 2** Reduction of Bi^{3+} into Bi

Fig. 3 The CV curve of selenium in acidic solution

reaction of direct reduction of H_2SeO_3 to H_2Se. This reaction (reaction 2) is obtained at a potential of the order of 30 mV (vs. SCE) and which is approximately the potential where the CV curve changes course for the second time (experimentally 60 mV (vs. SCE)) if a slight overvoltage of $H_2Se_{(g)}$ on FTO is accepted [27].

$$H_2SeO_3 + 6H^+ + 6e^- \leftrightarrows H_2Se_{(g)} + 3H_2O \qquad (3)$$

It is reported in the literature that a [26] reaction can take place between selenium oxidation state $+$ IV and $-$ II.

$$H_2SeO_3 + 2H_2Se_{(g)} \leftrightarrows 3Se_{(s)} + H_2O \qquad (4)$$
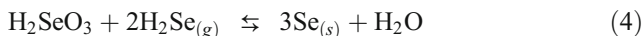
Above -280 mV (vs. SCE), the contribution of hydrogen reduction becomes important. From the above, it can be said that the optimal range of applied potential to obtain Bi_2Se_3 films, extends from -190 to -280 mV (vs. SCE). This potential range is similar to that proposed by Xiao-long Li et al. and others [28, 29]. Several co-deposition reactions of bismuth and selenium in the form of Bi_2Se_3 have been proposed. The main ones are as follows:

Selenium adsorbed on the substrate surface by reaction 5 reacts with Bi^{3+} as follows [28]:

$$2Bi^{3+} + 3Se + 6e^- \leftrightarrows Bi_2Se_3 \qquad (5)$$
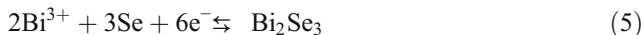
Based on studies on the electroplating of Bi_2Te_3 [10], another reaction seems plausible.

$$3H_2SeO_3 + 2Bi^{3+} + 12H^+ + 18e^- \leftrightarrows Bi_2Se_3 + 9H_2O \quad (6)$$
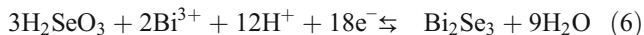
This type of reaction is widely proposed for the electrodeposition of other thermoelectric materials, such as Bi_2Te_3 as reported by Elyaagoubi et al. [30].

The anodic peak observed in the case of the mixture bismuth selenium solution (Fig. 1) can be attributed to the

dissolution of Bi_2Se_3 formed during the bismuth and selenium forward scan (Fig. 4) as reported in the literature [23, 26] or according to the reaction [31] (Eq. 7).

$$Bi_2Se_3 \leftrightarrows 3Se + 2Bi^{3+} + 6e^- \qquad (7)$$
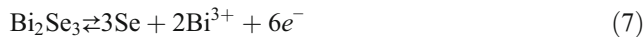
It is reported in the literature that when the potential decreases (moves cathodically), the film became richer in bismuth [32]. Thus, for a voltage of -150 mV (vs. SCE), the film is found to be rich in selenium, and at a voltage below -280 mV (vs. SCE), the film is rich in bismuth. Thus, we report in the following Table 1 the proportions of bismuth and selenium as a function of the deposition potential.

Therefore, theoretically, the range of applied potentials to obtain a Bi_2Se_3 composition can range between -190 and -280 mV (vs. SCE); for this, we have chosen the potentials -200 mV (vs. SCE) and -250 mV (vs. SCE).

When the deposition potential is between -200 and -250 mV (vs. SCE), the film adheres homogeneously and is gray in color. Nevertheless, the films obtained at more negative potential than -250 mV (vs. SCE) are black and peel off the substrate. In addition, in the exposed regions substrate (FTO), from which the film peeled off, a gas (certainly H_2) across the formed films evolved.

The chronoamperometric curves obtained for a stoichiometric mixture of $5 \cdot 10^{-3}$ M for 60 min under stirring and at a temperature of 30 °C are summarized in Fig. 5.

A sharp drop of the current density with time is seen, when the applied potential is -250 mV (vs. SCE), reaching a minimum value of -2 mA/cm^2. This value was reached after about 21 min of time recording. On the other hand, when we applied a voltage at about -200 mV (vs. SCE), there is a delay of 7 min before the nucleation process began, and the current decreases until reaching its low value of -1.05 mA/cm^2 after 39.5 min.
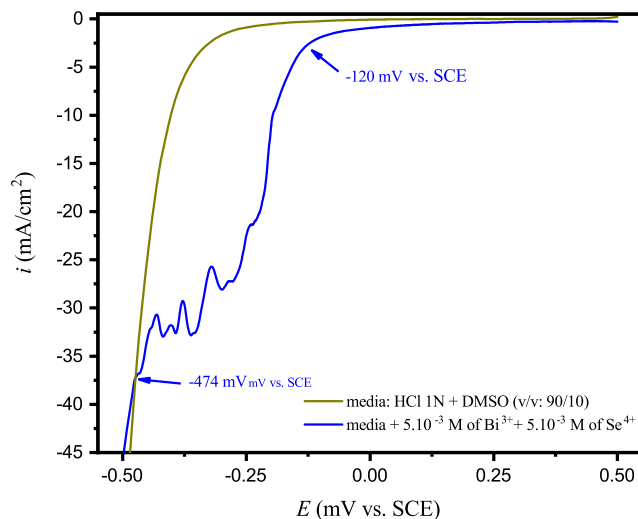

Fig. 4 The bismuth and selenium forward scan

Table 1 Evolution of selenium bismuth ratio with applied potential

E_{app} [mV vs. SCE]	− 150	− 200	− 250	− 300	− 350
*[Se]/[Bi]		7.9	1.65	1.58	1.38	1.0

*[Se]/[Bi] Is the ratio of atomic percentage found by EDX for both elements

These chronoamperometric curves show two zones, the first where a rapid drop in current occurs and reaches a minimum (i_m) which corresponds to the formation of the first nuclei (zone **I**). The active surface is, at this moment, reduced (surface coverage is maximal). A second zone (zone **II**) in which there is a slight increase in the current and which may correspond to the appearance of new nuclei and/or the growth of nuclei already formed [33, 34].

Figure 6 shows a comparison between the experimental and theoretical curves according to Sharifker et al. [35–37] for applied potentials of − 200 and − 250 mV (vs. SCE).

This nucleation is a mixture of two-dimensional progressive nucleation, and three-dimensional progressive thickening was observed in the case of − 200 mV (vs. SCE), and thus is expected to form layer on layer. Instantaneous and three-dimensional nucleation in the case of − 250 mV (vs. SCE) deposition potential was revealed.

At − 200 mV (vs. SCE) (Fig. 7a), the substrate surface is homogeneous, completely covered yet granular, with multilayer formation in the Z-direction. This finding corroborates the results of the growth kinetics of the formed films.

However, when the voltage is − 250 mV (vs. SCE), the film is compact and the grain size is larger compared with those obtained for − 200 mV (vs. SCE) (Fig. 7b). At high magnification, each grain randomly initiates nucleation. These nuclei are of the nanometric order (< 200 nm)
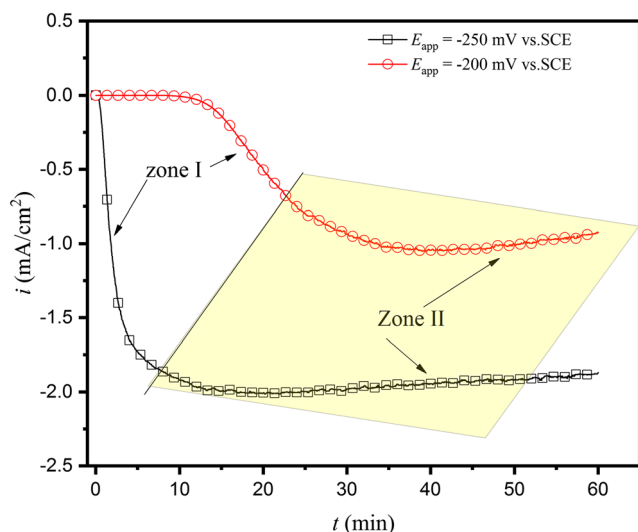

Fig. 5 The chronoamperometric curves obtained for a stoichiometric mixture of $5 \cdot 10^{-3}$ M
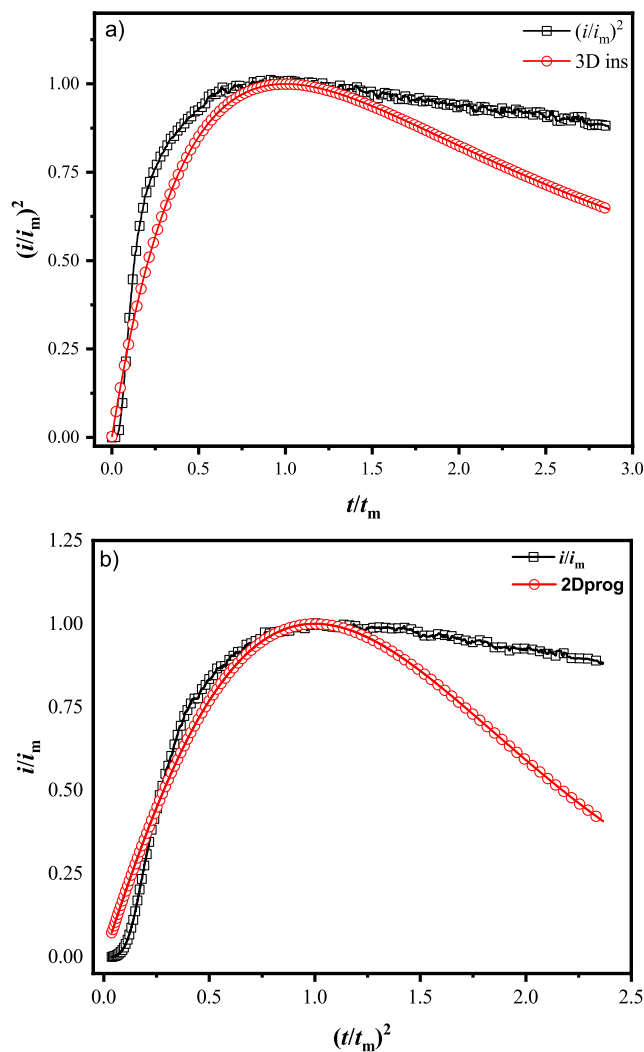

Fig. 6 Comparison between the experimental and theoretical curves according to Sharifker et al.

(Fig. 7c). The morphology of the films obtained is shown in Fig. 7.

The obtained films are characterized by X-ray diffraction. The DRX spectra of the two samples obtained at − 200 and − 250 mV (vs. SCE) for 1 h are shown in Fig. 8. It can be said that as the voltage decreases, the film thickness increases because of peaks relative to FTO disappeared.

Four new peaks that were not present in the substrate spectrum (FTO) can be observed. Two large peaks respectively centered at 24.2° and 43.9° may be attributed to the (101) and (110) reticular planes. Two intense peaks at 29.6° and 30.8°, both of which can be attributed to the (015) reticular plane, can be observed. The shape of the RDX spectra showed poor crystallinity of the formed films. The overlapping of the peaks relative to the substrate and those of the formed film, makes it difficult to pronounce on the nature of the formed film. For this reason, characterization of the formed film was carried out using grazing incidence X-ray diffraction. Figure 9
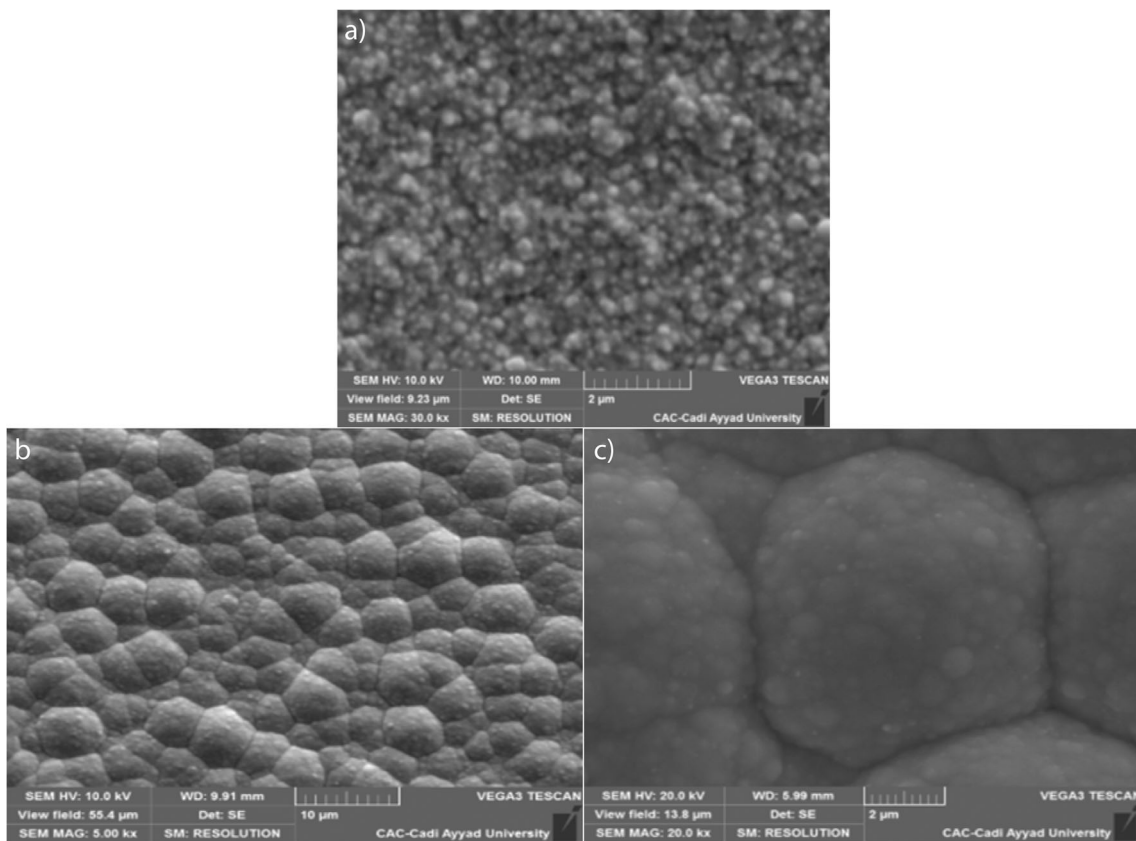
Fig. 7 Morphology of the films

presents the grazing X-ray diffraction spectrum of a samples obtained at − 200 mV and − 250 mV (vs. SCE) for 1 h.

Three peaks can be distinguished at 24.3°, 29.57°, and at 43.6 degrees which are characteristic of the Bi_2Se_3
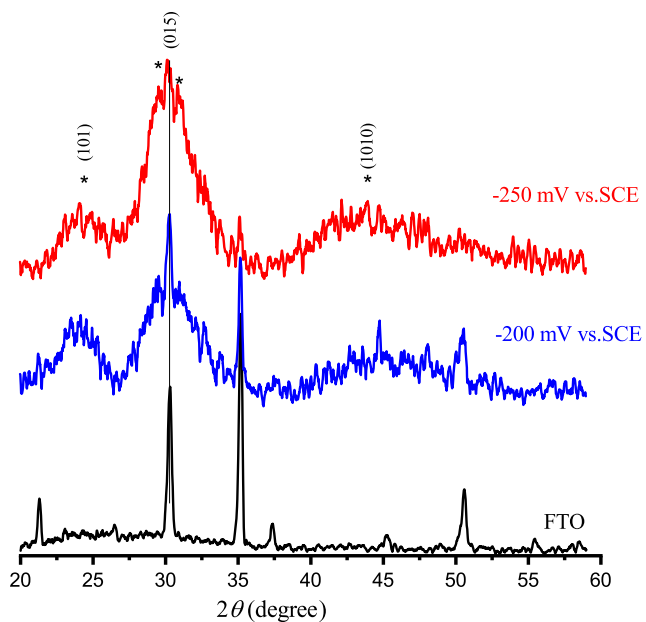
Rhombohedral phase according to the standard JCPDS sheet (00-033-0214 and 01-89-2008). These results are in perfect agreement with those reported in the literature [17, 38–40].

At the same figure (Fig. 9), we note the presence of peaks at 30.2° and 50.3° for sample obtained at − 200 mV vs. SCE, which seems to be due according to Ahmed Rasin et al. to the
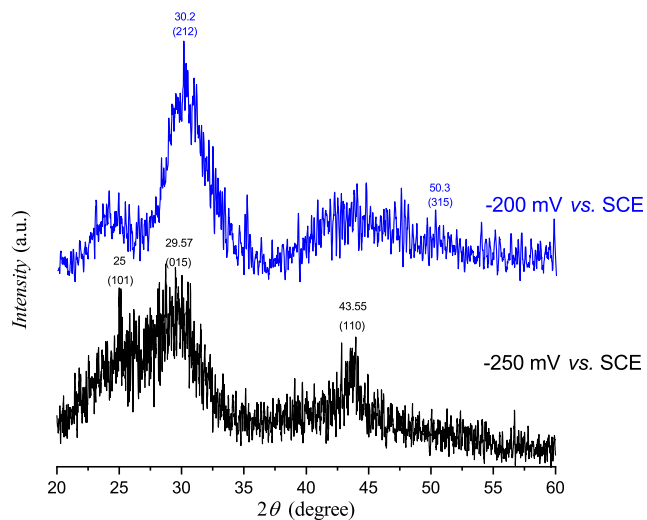

Fig. 8 DRX spectra of the two samples obtained at − 200 and − 250 mV (vs. SCE)

Fig. 9 The grazing X-ray diffraction spectrum of a samples obtained at − 200 mV and − 250 mV (vs. SCE)

presence of the orthorhombic metastable phase of Bi2Se3 [10, 17, 27].

The Raman spectrum for the samples obtained at − 200 and − 250 mV (vs. SCE) is shown in Fig. 10. The film obtained at − 250 mV (vs. SCE) has three distinct bands, while the film obtained at − 200 mV (vs. SCE) has more than six bands.

The bands observed in the case of − 250 mV (vs. SCE) are 73.3, 132, and 177 cm^{-1} which may be attributed respectively to the vibration modes $A_{1g}^{(1)}$; $E_g^{(1)}$, and $A_g^{(2)}$ and which are characteristic of the rhombohedral phase. Moreover, the Raman spectrum of the film obtained at − 200 mV (vs. SCE) reveals the presence of three peaks and three shoulders: the three peaks are centered at 73.3; 130.6, and 158.9 cm^{-1}, and shoulders centered at 63.6, 80.7, and 170.3 cm^{-1}.

Peaks at 73.3, 130.6, and the shoulder at 170.3 can be attributed respectively to the vibration modes $A_{1g}^{(1)}$, $E_{2g}^{(2)}$, and $A_g^{(2)}$. The peak centered at 158.9 cm^{-1} is assigned to the vibration mode $A_1^{(3)}$. This vibration mode is relative to the orthorhombic phase of the metastable Bi$_2$Se$_3$ or to the nanostructured surface reasoning. The shoulders of low intensities observed at 63 and 80.7 were respectively attributed to the $A_1^{(1)}$ and $E_u(1)$ vibration modes. The presence of shoulders and the Raman shift to low values is certainly due to the co-presence of the two orthorhombic (O-Bi$_2$Se$_3$) and rhombohedral phases (r-Bi$_2$Se$_3$). This conclusion is corroborated by the presence of the band at 160 cm^{-1} which is characteristic of the orthorhombic phase of Bi$_2$Se$_3$. We summarized in the Table 2 below the different wavenumbers of the bands emerging from the Raman spectra, and their modes of vibration. Results given by the Raman analysis are in good agreement with those obtained by grazing X-ray diffraction.
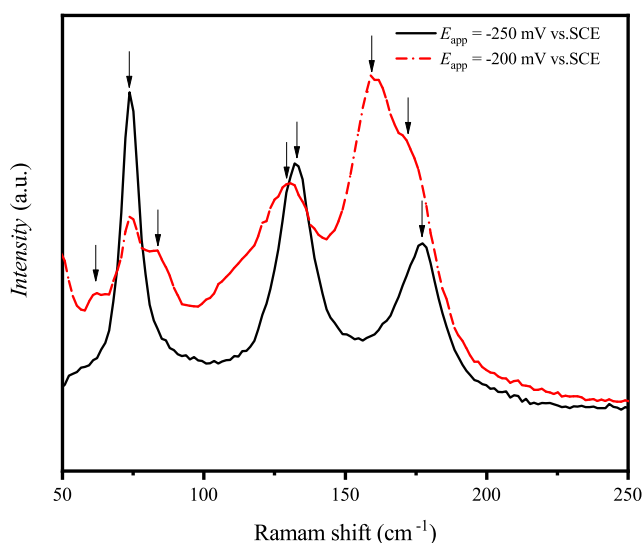
Table 2 Raman active vibration mode attribution

Vibrational frequency (cm^{-1})	Attribution	Ref
63	$A_1^{(1)}$	[41]
74	$A_{1g}^{(1)}$	[11, 42–45]
84	$E_u^{(1)}$	[46]
130–132	$E_{2g}^{(2)}$	[11, 41, 43, 44, 47]
160	$A_1^{(3)}$ and/or A_{2u}	[11, 17, 41]
177	$A_{1g}^{(2)}$	[11, 41, 43, 44]

The presence of vibration mode, like A_{2u} and E_u Raman inactive modes, can be explained by missing of the crystallinity of Bi$_2$Se$_3$ [47].

The conductive behavior of the formed films was studied by plotting the variation of $1/C^2$ as a function of the voltage applied in 0.1 M Na$_2$SO$_4$ at a frequency of 1 kHz. Indeed, the measured capacitance C can be considered a series combination of two contributions:

$$1/C = 1/C_{SC} + 1/C_{dl} \qquad (8)$$

where C_{sc} is the space charge capacitance of the film and C_{dl} is the capacitance of the double layer, which is usually orders of magnitude higher than C_{sc} given by the Mott-Schottky relationship:

$$\frac{1}{C_{sc}^2} = \frac{2}{\varepsilon_r \varepsilon_0 e N_d}\left(E - E_{fb} + \frac{KT}{e}\right) \qquad (9)$$

where ε_r is the dielectric constant of the formed film, ε_0 is the permittivity of the vacuum (8.854×10^{-14} F cm^{-1}), e is the absolute charge, E_{fb} is the flat-band potential, K is the Boltzmann constant (1.38×10^{-23} J/K), N_d is the donor

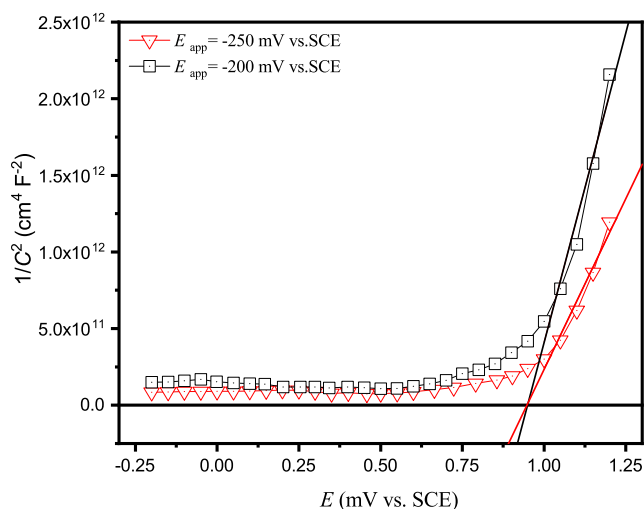**Fig. 10** The Raman spectrum for the samples obtained at − 200 and − 250 mV (vs. SCE)

Fig. 11 The shapes of the variation of $1/C^2$ against potential, for the films obtained at − 200 and − 250 mV (vs. SCE)

Table 3 Evolution of charge carriers and flat band with applied potential

Permittivity		Applied potential (vs. SCE)	
		− 0.2 V	− 0.25 V
29	Charge carriers ($N_d \times 10^{17}$ cm^{-3})	6	11
16.3		10	20
29	Flat-band potential (V vs. SCE)	0.95	0.94
16.3		0.95	0.94

concentration in the case of an n-type semiconductor, and T is the absolute temperature.

The variation of $1/C^2$ as a function of potential referenced to saturated calomel electrode (SCE) allows therefore the determination of N_d, which is also equal to the charge carrier density room temperature, and also the flat-band potential from the linear part of this curve. The latter parameter is the potential required to counterbalance the potential drop originating from the space charge in the semiconductor that results from the semiconductor/electrolyte junction. The space charge, which is responsible for the band bending, occurs as a result of the charge-transfer between the semiconductor and the electrolyte redox couple that is required to align the Fermi levels.

The shapes of the variation of $1/C^2$ against potential, for the films obtained at − 200 and − 250 mV (vs. SCE) are shown in Fig. 11.

From these curves, we can say that the formed films are n-type semiconductors. The exploitation of these curves allowed us to determine the density of the charge carriers and also the flat-band potential. In order to do this, we need to know the permittivity of the formed film.

A value between 16.3 and 29 has been reported in the literature [48, 49]. With this range of values, the table below (Table 3) shows the values for the potential of the flat band and the number of charge carriers:

From these results, it can be concluded that the number of charge carriers doubles from − 200 to − 250 mV (vs. SCE). Moreover, these values remain of the same order of magnitude as those related from the literature [50]. The values of flat-band potentials seem to be higher than those reported in the literature [51, 52]. This may be due to the fact that we have neglected the contribution of the double-layer capacitance in the overall capacitance.

Conclusion

The study of the electrodeposition of bismuth and selenium films reveals that the desired Bi$_2$Se$_3$ stoichiometry is obtained when the imposed potential is about − 250 mV (vs. SCE). Indeed, the stoichiometry depends on the imposed potential.

The more cathodic is the potential, the richer the formed film is in bismuth. This conclusion was supported by X-ray diffraction analysis, which shows the presence of a rhombohedral phase of Bi$_2$Se$_3$, Raman spectroscopy supports this suggestion, since the peaks found are those of r-Bi$_2$Se$_3$. The possibility of the formation of O-Bi$_2$Se$_3$ is also considered. The films obtained are n-type semiconductors, and the number of charge carriers is in the order of 10^{18} cm^{-3}.

Compliance with ethical standards

Conflict of interest The authors declare that they have no conflicts of interest.

References

1. Waters J, Crouch D, Raftery J, O'Brien P (2004) Deposition of bismuth chalcogenide thin films using novel single-source precursors by metal-organic chemical vapor deposition. Chem Mater 16(17):3289–3298

2. Li J, Jiang F, Yang B et al (2013) Topological insulator bismuth selenide as a theranostic platform for simultaneous cancer imaging and therapy. Sci Rep 3:1–7

3. O'Neal DP, Hirsch LR, Halas NJ et al (2004) Photo-thermal tumor ablation in mice using near infrared-absorbing nanoparticles. Cancer Lett 209(2):171–176

4. Zhang XD, Jing Y, Song S, Yang J, Wang JY, Xue X, Min Y, Park G, Shen X, Sun YM, Jeong U (2017) Catalytic topological insulator Bi$_2$Se$_3$ nanoparticles for in vivo protection against ionizing radiation. Nanomed Nanotechnol Biol Med 13(5):1597–1605

5. Desai ND, Ghanwat VB, Khot KV et al (2016) Effect of substrate on the nanostructured Bi2Se3 thin films for solar cell applications. J Mater Sci Mater Electron 27:2385–2393

6. Liu S, Huang Z, Qiao H, Hu R, Ma Q, Huang K, Li H, Qi X (2020) Two-dimensional Bi2Se3 nanosheet based flexible infrared photodetector with pencil-drawn graphite electrodes on paper. Nanoscale Adv 2(2):906–912

7. Kong D, Randel JC, Peng H, Cha JJ, Meister S, Lai K, Chen Y, Shen ZX, Manoharan HC, Cui Y (2010) Topological insulator nanowires and nanoribbons. Nano Lett 10(1):329–333

8. Li LL, Xu W (2015) Thermoelectric transport by surface states in Bi2Se3-based topological insulator thin films. Chin Phys Lett 32(4):047304

9. Nechaev IA, Hatch RC, Bianchi M, Guan D, Friedrich C, Aguilera I, Mi JL, Iversen BB, Blügel S, Hofmann P, Chulkov EV (2013) Evidence for a direct band gap in the topological insulator bi 2Se3 from theory and experiment. Phys Rev B - Condens Matter Mater Phys 87(12):121111

10. Tumelero MA, Benetti LC, Isoppo E, Faccio R, Zangari G, Pasa AA (2016) Electrodeposition and ab initio studies of metastable orthorhombic Bi2Se3: a novel semiconductor with bandgap for photovoltaic applications. J Phys Chem C 120(22):11797–11806

11. Souza PB, Tumelero MA, Zangari G, Pasa AA (2017) Tuning electrodeposition conditions towards the formation of smooth Bi2Se3 thin films. J Electrochem Soc 164:D401–D405

12. Wei ZT, Zhang M, Yan Y, Kan X, Yu Z, Chen YL, Yang XS, Zhao Y (2015) Transport properties of Bi2Se3 thin films grown by magnetron sputtering. Funct Mater Lett 8(02):1550020

13. Zhang M, Wei Z, Jin R, Ji Y, Yan Y, Pu X, Yang X, Zhao Y (2016) Electrical transport properties and morphology of topological insulator Bi2Se3 thin films with different thickness prepared by magnetron sputtering. Thin Solid Films 603:289–293

14. Ota JR, Roy P, Srivastava SK, Popovitz-Biro R, Tenne R (2006) A simple hydrothermal method for the growth of Bi2Se3 nanorods. Nanotechnology 17(6):1700–1705

15. Bin MK, Kumar P, Giri R, Singh J (2020) Controlled synthesis of two-dimensional (2-D) ultra-thin bismuth selenide (Bi2Se3) nanosheets by bottom-up solution-phase chemistry and its electrical transport properties for thermoelectric application. FlatChem 21: 100165

16. Liu H, Cui H, Han F, Li X, Wang J, Boughton RI (2005) Growth of Bi2Se3 nanobelts synthesized through a co-reduction method under ultrasonic irradiation at room temperature. Cryst Growth Des 5(5): 1711–1714

17. Ahmed R, Xu Y, Sales MG, Lin Q, McDonnell S, Zangari G (2018) Synthesis and material properties of Bi2Se3 nanostructures deposited by SILAR. J Phys Chem C 122(22):12052–12060

18. Gupta S, Singh R, Anoop MD et al (2019) Optical studies on bismuth chalcogenides. Mater Today: Proc 10:142–150

19. Jana A, Datta J (2013) Enhancement of photo-characteristics of Bi2Se3 thin films by post heat treatment at optimal temperature range. J Electroanal Chem 689:31–41

20. Peng H, Zhou J, Tang D, Lai Y, Liu F, Li J, Liu Y (2011) Preparation and characterization of Bi2Se3 nanowires by electrodeposition. Electrochim Acta 56(14):5085–5089

21. Desai JD (1999) Galvanostatic electrodeposition of Bi2Se3 thin films. Bull Electrochem 15:315–317

22. Pourbaix M (1964) Atlas D'equilibres electrochimiques. Gauthier-V

23. Ham S, Jeon S, Park M, Choi S, Paeng KJ, Myung N, Rajeshwar K (2010) Electrodeposition and stripping analysis of bismuth selenide thin films using combined electrochemical quartz crystal microgravimetry and stripping voltammetry. J Electroanal Chem 638(2):195–203

24. Ouahine H, Hasnaoui A, Hdoufane I, Idouhli R, Abouelfida A, Ait Ali M, el Firdoussi L (2020) Benzo[c][1,2,5]selenadiazole organoselenium derivatives: synthesis, X-ray, DFT, Fukui analysis and electrochemical behavior. J Mol Struct 1199:126914

25. Li J, Wang B, Liu F, Yang J, Li J, Liu J, Jia M, Lai Y, Liu Y (2011) Preparation and characterization of Bi-doped antimony selenide thin films by electrodeposition. Electrochim Acta 56(24):8597–8602

26. Li J, Jiang L, Wang B, Liu F, Yang J, Tang D, Lai Y, Li J (2013) Electrodeposition and characterization of copper bismuth selenide semiconductor thin films. Electrochim Acta 87:153–157

27. Ahmed R, Lin Q, Xu Y, Zangari G (2019) Growth, morphology and crystal structure of electrodeposited Bi2Se3 films: influence of the substrate. Electrochim Acta 299:654–662

28. Li XL, Cai KF, Li H, Wang L, Zhou CW (2010) Electrodeposition and characterization of thermoelectric Bi2Se3 thin films. Int J Miner Metall Mater 17(1):104–107

29. Salazar-Banda GR, Solaliendres MO, Manzoli A et al (2008) The processes involved in the se electrodeposition and dissolution on Au electrode: the H 2Se formation. J Solid State Electrochem 12: 679–686

30. Elyaagoubi M, Najih Y, Khadiri M et al (2017) Electrochemically deposited bismuth-telluride nanowires in nanoporous alumina membranes. J Mater Environ Sci 8:2070–2075

31. Mao S, Zhang S, Niu H, Song J, Jin B, Wu J, Tian Y (2011) Synthesis and electrochemical property of Bi2Se3 nanotubes with laminar surface. J Nanosci Nanotechnol 11(3):2064–2069

32. Zhang X, Liang X, Xu M, Bao X, Wang F, Yang Z (2012) Electrodeposit nano-copper oxide on glassy carbon electrode for simultaneous detection of guanine and adenine. J Appl Electrochem 42(6):375–381

33. Mendoza-Huizar LH, Robles J, Palomar-Pardavé M (2003) Nucleation and growth of cobalt onto different substrates - part II. The upd-opd transition onto a gold electrode. J Electroanal Chem 545:39–45

34. de Regt JM, Dijk J, Mullen JAM et al (1995) Components of continuum radiation in an inductively coupled plasma. J Phys D Appl Phys 28(1):40–46

35. Scharifker BR, Hills G (1983) Theoretical and experimental studies of multiple nucleation. Electrochim Acta 28(7):879–889

36. Milchev A, Krastev I (2011) Two-dimensional progressive and instantaneous nucleation with overlap: the case of multi-step electrochemical reactions. Electrochim Acta 56(5):2399–2403

37. Bento FR, Mascaro LH (2002) Analysis of the initial stages of electrocrystallization of Fe, Co and Fe-Co alloys in chloride solutions. J Braz Chem Soc 13:502–509

38. Cai KF, Wang L, Yin JL, Zhou CW (2008) Synthesis and characterization of Bi2Se3 thermoelectric nanopowders

39. Indirajith R, Rajalakshmi M, Gopalakrishnan R, Ramamurthi K (2016) Characterization of bismuth selenide (Bi2Se3) thin films obtained by evaporating the hydrothermally synthesised nano-particles. Superlattice Microst 91:165–172

40. El-Nahass MM, Zeyada HM, Aziz MS, El-Ghamaz NA (2004) Structural and optical properties of thermally evaporated zinc phthalocyanine thin films. Opt Mater (Amst) 27(3):491–498

41. Kung HH, Salehi M, Boulares I, Kemper AF, Koirala N, Brahlek M, Lošťák P, Uher C, Merlin R, Wang X, Cheong SW, Oh S, Blumberg G (2017) Surface vibrational modes of the topological insulator Bi2Se3 observed by Raman spectroscopy. Phys Rev B 95(24):245406

42. Sahoo S, Gaur APS, Ahmadi M, Guinel MJF, Katiyar RS (2013) Temperature-dependent Raman studies and thermal conductivity of few-layer MoS2. J Phys Chem C 117(17):9042–9047

43. Richter W, Becker CR (1977) A Raman and far-infrared investigation of phonons in the rhombohedral V2–VI3 compounds Bi2Te3, Bi2Se3, Sb2Te3 and Bi2(Te1−xSex)3 (0 < x < 1), (Bi1−ySby)2Te3 (0 < y < 1). Phys Status Solidi 84(2):619–628

44. Yuan J, Zhao M, Yu W, Lu Y, Chen C, Xu M, Li S, Loh K, Qiaoliang B (2015) Raman spectroscopy of two-dimensional Bi2TexSe3-x platelets produced by solvothermal method. Materials (Basel) 8(8):5007–5017

45. Cheng T, Tan C, Zhang S, Tu T, Peng H, Liu Z (2018) Raman spectra and strain effects in bismuth oxychalcogenides. J Phys Chem C 122(34):19970–19980

46. Gnezdilov V, Pashkevich YG, Berger H, Pomjakushina E, Conder K, Lemmens P (2011) Helical fluctuations in the Raman response

of the topological insulator Bi2Se3. Phys Rev B - Condens Matter Mater Phys 84(19):195118

47. Shahil KMF, Hossain MZ, Goyal V, Balandin AA (2012) Micro-Raman spectroscopy of mechanically exfoliated few-quintuple layers of Bi2Te3, Bi2Se3, and Sb2Te3 materials. J Appl Phys 111(5):054305

48. Lawal A, Shaari A, Ahmed R et al (2017) Electronic and optical properties of Bi2Se3 topological insulator: a promising absorbing layer for broadband photodetector. ARPN J Eng Appl Sci 12:5880–5886

49. Cao T, Wang S (2013) Topological insulator metamaterials with tunable negative refractive index in the optical region. Nanoscale Res Lett 8:1–8

50. Inhofer A, Duffy J, Boukhicha M et al (2018) Rf quantum capacitance of the topological insulator Bi2Se3 in the bulk depleted regime for field-effect transistors. Phys Rev Appl 9:024022

51. Ma L, Yang C, Tian X, Nie Y, Zhou Z, Li Y (2018) Enhanced usage of visible light by BiSex for photocatalytic degradation of methylene blue in water via the tunable band gap and energy band position. J Clean Prod 171:538–547

52. Xiao L, Liu Q, Zhang M, Liu L (2020) Photoelectric properties of Bi2Se3 films grown by thermal evaporation method. Mater Res Express 7(1):16429